REPORT DOCUMENTATION PAGE

Form Approved OMB No. 0704-0188

1. REPORT DATE *(DD-MM-YYYY)*	2. REPORT TYPE	3. DATES COVERED *(From – To)*
Feb 2006	Final Report	3 June 2005 - 03-Jun-06

4. TITLE AND SUBTITLE

New Techniques for Space Weather Forecasting: MoVaTrac: A Multiscale Optical Flow Algorithm Analyzing the dynamics in Solar EUV Images

5a. CONTRACT NUMBER
FA8655-05-M-4021

5b. GRANT NUMBER

5c. PROGRAM ELEMENT NUMBER

6. AUTHOR(S)

Dr. Jean-Francois Hochedez

5d. PROJECT NUMBER

5d. TASK NUMBER

5e. WORK UNIT NUMBER

7. PERFORMING ORGANIZATION NAME(S) AND ADDRESS(ES)

Royal Observatory of Belgium
Circular Avenue, 3
Brussels B1180
Belgium

8. PERFORMING ORGANIZATION REPORT NUMBER

N/A

9. SPONSORING/MONITORING AGENCY NAME(S) AND ADDRESS(ES)

EOARD
PSC 802 BOX 14
FPO 09499-0014

10. SPONSOR/MONITOR'S ACRONYM(S)

11. SPONSOR/MONITOR'S REPORT NUMBER(S)
SPC 05-4021

12. DISTRIBUTION/AVAILABILITY STATEMENT

Approved for public release; distribution is unlimited.

13. SUPPLEMENTARY NOTES

14. ABSTRACT

This report results from a contract tasking Royal Observatory of Belgium as follows: The Grantee will investigate novel methods for predicting the arrival of Coronal Mass Ejections (CMEs) using a series of solar images of Extreme Ultraviolet (UV) light. The aim of the research will be to establish image characteristics and pattern recognition sequences in predicting CMEs.

15. SUBJECT TERMS

EOARD, Magnetosphere, Space Weather, Ionosphere, Solar Physics

16. SECURITY CLASSIFICATION OF:			17. LIMITATION OF ABSTRACT	18, NUMBER OF PAGES	19a. NAME OF RESPONSIBLE PERSON
a. REPORT	b. ABSTRACT	c. THIS PAGE			MICHAEL KJ MILLIGAN, Lt Col, USAF
UNCLAS	UNCLAS	UNCLAS	UL	29	19b. TELEPHONE NUMBER *(Include area code)* +44 (0)20 7514 4955

MoVaTrac: A Multiscale Optical Flow Algorithm Analyzing the Dynamics in Solar EUV images

S. F. Gissot and J.-F. Hochedez

February 2006

Contents

1 Introduction

Movies of the Solar atmosphere reveal motions and variations of brightness. In particular a sequence of two coronal images may exhibit the plane-of-the-sky component of the speed combined with variation of the signal. The present work focuses on solar extreme-ultraviolet images as produced by the Extreme ultraviolet Imaging Telescope (EIT) aboard the Solar Heliospheric

Observer (SoHO). Our aim is to estimate both the apparent motion vector and the variation of brightness from two successive images. The Motion and brightness Variation Tracking (MoVaTrac) algorithm is based on a multi-scale optical flow algorithm derived from a local gradient-based technique. We demonstrate a new differential rotation measurement technique and the identification of coronal events as outliers to the differential rotation or as regions exhibiting a significant brightness variation. Space weather services have motivated this study. The range of potential interests includes but also extends beyond early warnings of flares and coronal mass ejection (CME) onsets. It includes for example studies of nanoflares or macrospicules, coronal seismology, MHD and EIT wave investigations, etc.

1.1 New Challenges in Space Weather Forecasting

The study of solar activity is needed for the protection of satellites, human space activities, etc. Scientists investigate the influences of solar events -flares and Coronal Mass Ejections (CMEs)- on the Earth environment. One crucial task in space weather applications consists in predicting major geomagnetic disturbances from the observation of the Sun corona and in situ records in the interplanetary space. Expert observers are carrying out the forecast, by especially using extreme ultraviolet coronal images from the Extreme ultraviolet Imaging Telescope (EIT, Delaboudiniere et al. (1995)) instrument aboard SoHO (Solar and Heliospheric Observatory). Early CME signatures include intensity variations in EUV images such as dimmings, EIT Waves, or motions such as loop openings and prominence eruptions. Since CMEs can cause geomagnetic storms, a fast detection of these signatures is very usefull to the space weather forecasters. Improving the prevision of geomagnetic disturbances from solar observations is a crucial task for space weather forecast centers. In the low corona, CME onset signatures include filament eruptions, coronal dimmings, EIT waves, loop openings, post-eruption arcades observed in the EUV and sigmoid-to-arcade restructuring in soft X-rays (Hudson & Cliver, 2001). Unfortunately, image processing of solar EUV image sequences is difficult. The main problems stem from the noise, the variations in source brightness discussed in Sect. 1.2, the swift and hence under-sampled topological changes, the lack of spatial resolution (spatial aliasing) and the transparency.

1.2 Dynamics in the Corona

The dynamic nature of the solar atmosphere has been observed and modeled (Rosner et al., 1978; Moses et al., 1997; Schrijver et al., 1999). The re-

cent years have accentuated the irrelevance of stasis in studying the physics of the chromosphere, transition region and corona. Dynamics is concerned with the effects of forces upon motion. Reciprocally, the knowledge of movements and accelerations must constrain the models, validating or falsifying consequently the underlying physics. While forces are invisible, motion can be quantitatively estimated by observational means. Both spectroscopy and image sequences can reveal motion. Spectroscopy informs on the line-of-sight (LOS) velocity component for traveling plasma, whilst movies exhibits only the transversal component of the speed. Both approaches have their respective advantages and restrictions, but they are complementary when the two types of observations coincide (e.g. Kucera et al., 2003). The shifts must in that case be of the order of the resolution element, i.e. *macroscopic*. The present work deals only with the second method. It specially focuses on solar extreme ultraviolet (EUV) images as produced in surfeit by EIT (Delaboudiniere et al., 1995) on board SoHO (see for instance Fig. 1), TRACE (Handy et al., 1999) or SPIRIT-CORONAS (Oraevsky & Sobelman, 2002). Yet, the presented developments has the potential to be applied on magnetographic, photospheric and coronographic image sequences or future data such as SWAP/Proba2, AIA/SDO or SECCHI/STEREO.

Introducing the concept of *apparent motion* states immediately a fundamental limitation of imaging data: images are projections in the $2D$ plane of the sky of $3D$ features. This problem of perspective in the mostly transparent corona creates not only geometrical distortions of the velocity fields but also ambiguities if more than one "feature" superimpose on the LOS. It also generates annoying occultations where opaque objects such as prominences or the solar disc itself are considered. However, apparent motion goes beyond mere projection effects: motion tracking algorithms, as well as human observers, can trace only intensity patterns but not actual plasma blobs. Without spectroscopic information, propagating brightness patterns are *a priori* indistinguishable from actual motions (De Groof et al., 2004). Fortunately, at the same time, this ambiguity gives access to a range of wave phenomena able to bring physical insights of their own (e.g. Deforest & Gurman, 1998; Klimchuk et al., 2004). Noglik et al. (2005) calculate the reconnection rate from the estimated velocity at which successive loops brighten.

Nevertheless, solar rotation dominates the motion in image sequences. Recent works (e.g. Brajša et al., 2001; Vršnak et al., 2003) have studied differential rotation in various layers of the atmosphere. The present report uses their results for calibration purposes. In a future publication, our method eases the survey of solar rotation over long periods. After differential rotation compensation, residual motion brings a wealth of insights. Coronal activity is obviously not limited to mere topological evolutions and rearrangements.

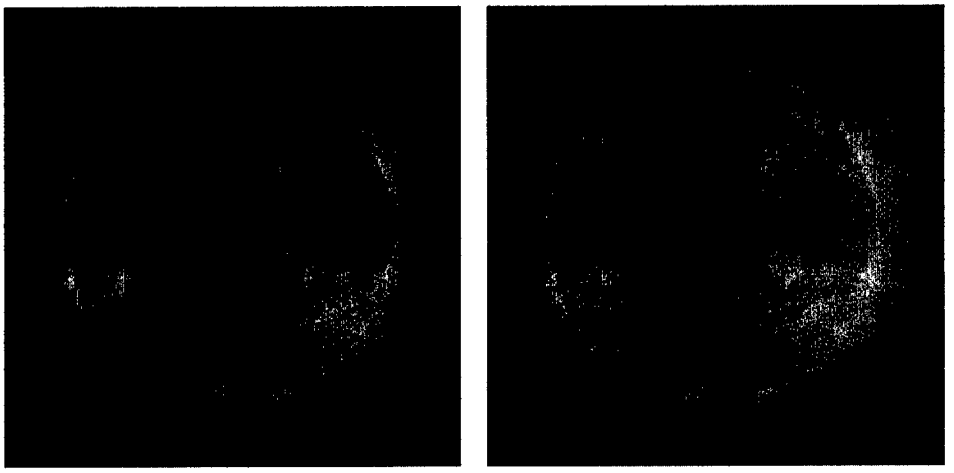

a. EIT image J_1. b. EIT image J_2.

Figure 1: A sequence of two successive EIT images observed on 1998-05-03, repectively at times 21:00:21 (I_1) and 21:12:09 (I_2) in the CME Watch mode, at the wavelength 19.5 nm.

Temperature and density variations are ubiquitous. When they combine with instrumental passbands, the observed volumes of plasma brighten or darken. As long as too few bandpasses are recorded, the differential emission measure (DEM) cannot be recovered and it is necessary to separate motion from brightness variations (BV). We will see in Sect. 2.3.1 the required conditions for such disentanglement.
Estimating both speed and brightness variations in parallel is mathematically logical and also physically meaningful; solar activity exhibits both motion and brightenings, flaring and dimmings. A technique capable of producing velocity and BV maps addresses essentially all phenomena seen in imaging data. Space weather services have motivated this study (e.g. Hochedez et al., 2005), although the range of potential interests extends beyond early warnings of flares and Coronal Mass Ejection (CME) onsets. It includes for example studies of nanoflares or macrospicules, coronal and seismology, MHD and EIT wave investigations, etc.

1.3 EUV Sequence Analysis of the Solar Corona

There exist three main classes of methods for motion analysis of a sequence of *two* images (Barron et al., 1992) : gradient-based (local or global), matching-based and feature-based. Gradient-based and matching-based, such as Local Correlation Tracking (LCT) are said to be *dense*, contrary to feature-based

methods, in the sense that they provide an estimation of the velocity at every pixel and not only at sparse features. Dense does not mean that the quality of the estimation is uniform over the image, and we expect that some solar regions have better estimations, since motion is better defined at these locations. In feature-based methods, the extraction of the features is a problematic preprocessing step.

Several authors have proposed matching techniques based on the local correlation tracking (LCT) for sequences of solar images at the photospheric level (November & Simon, 1988; Welsch et al., 2004). This technique has also been modified by Roudier et al. (1999) and applied to TRACE photospheric data (see Krijger et al., 2002; Krijger & Roudier, 2003). In order to process vector magnetograms, Longcope (2004) estimates the velocity by minimizing an energy term. Their "minimum energy fit" enforces consistency with the magnetic induction equation. All these techniques deal with photospheric velocity flows.

To our knowledge and apart from our early results (Gissot et al., 2003), dense velocity field estimations, have not been calculated from EUV sequences of the corona. Brajša et al. (2001) uses a feature-based method to track bright points and point-like structures (PLS). Each feature is a point in the $(\mathrm{b}, \omega_{\mathrm{rot}})$ plane where b is the heliospheric latitude and ω_{rot} is the angular velocity. The authors then fit a parametric model of differential rotation through the cloud of feature points. This method is sensitive to the reliability of the feature extraction. In this report, we present a multiscale optical flow (OF) algorithm derived from the work of Lucas & Kanade (1981) (LK), which states a local gradient-based technique. Our aim is to estimate both the fields of apparent displacement and brightness variation from two successive images.

We further demonstrate a new differential rotation measurement and the identification of coronal events as outliers to the differential rotation or as regions exhibiting a significant BV. We apply the algorithm on EIT sequences of May 3, 1998 (Fig. 1) and April 17, 1999, that have been observed during the CME Watch observation mode at the wavelength 19.5 nm (Fe XII spectral emission line). The report is organized as follows : in Sect. 2, we present the formulation of our new method of motion analysis. In Sect. 3, we show the results of the calibration of the method on synthetic signals and discuss the analysis of observations in Sect. 4.

2 MovaTrac: A New Algorithm Analyzing Sequences of EUV coronal Images

In order to calculate the coordinates of the velocity vector for each pixel, we can establish the optical flow (OF) using the brightness constancy assumption (BCA). The BCA (Horn & Schunck, 1981) states that the source of intensity remains constant over time. This provides a single equation per pixel –the optical flow constraint equation (OFCE)– while there are two unknowns, namely the 2 velocity vector coordinates. This is the *aperture problem.* To solve this under-determination, following Lucas & Kanade (1981), we further assume the local uniformity of the velocity field in the neighborhood of a pixel. An alternative approach would be to solve globally and iteratively until convergence of the velocity field (Horn & Schunck, 1981) by adding a constraint on its smoothness. The disadvantage of this other method is that bad estimations can propagate to the rest of the image through the smoothing. Furthermore a local diagnostic on the quality of the estimation is impossible because the solution is global. Other important approaches to optical flow computation are probabilistic (Simoncelli et al., 1991; Simoncelli, 1999) or robust minimization (Black & Anandan, 1993). In our algorithm, we extend the BCA and the OFCE to estimate both the velocity and the brightness variation (BV) fields in the special case of coronal ultraviolet images. To this end, a *multiscale* computation of the flow iterates the estimation from an upper scale to a lower scale, the scale being the size of the neighborhood of observation. The estimation is updated *if* a *quality* index for the estimation, that we define in Sect. 2.3.1, is improved across scales. In this section, after describing the preprocessing that we apply to the images (Sect. 2.1), we introduce our new symmetric optical flow equations (SOFA, see Sect. 2.2.3). It induces a symmetry constraint between the first and the second image and we can express the estimation in the Bayesian framework.

2.1 Sequence Preprocessing

First we remove the cosmic ray hits (CRH) using a median filter (this procedure is part of the solar soft library). We apply a logarithmic transform to bring out the low-intensity part of the signal. Finally, we apply a gaussian smoothing to the image before computation. This step allows us to compute robust spatial gradient estimations, and is also important to remove the estimation biases. Thus, if we note g the gaussian kernel of our smoothing, our

signal becomes $\tilde{I}_D = g_a \star I_D$. The spatial derivatives are

$$\begin{aligned}\frac{\partial \tilde{I}_D}{\partial x} &= \frac{\partial}{\partial x}(g_a \star I_D) \\ &= \frac{\partial g_a}{\partial x} \star I_D \\ &= < g_{1,a}, I_D >\end{aligned}$$

Similarly we have :

$$\frac{\partial \tilde{I}_D}{\partial y} =< g_{2,a}, I_D >$$

We have access to an analytical derivative of the preprocessed signal $\tilde{I} = g_a \star I$ where a is the scale of the gaussian function $g_a(\vec{x}) = \frac{1}{2\pi a^2} \exp(-\frac{\vec{x}^2}{2a^2})$. The analytical expression of the gradient is given by:

$$\nabla \tilde{I} = (\frac{\partial \tilde{I}}{\partial x}, \frac{\partial \tilde{I}}{\partial y}) = (\frac{\partial g}{\partial x} \star I, \frac{\partial g}{\partial y} \star I).$$

2.2 The optical flow equations

There are two equivalent formulations of the OFCE: partial differential equation (PDE) and image registration. We aim at estimating the deformation, if small enough, between the first image I_1 and the second I_2. The PDE formulation is detailed in appendix (Sect. A).

2.2.1 Image Registration

We note $\vec{x} = (x, y)^{\mathrm{T}}$ is the spatial position in the image plane (plane-of-sky).

We can formulate the BCA as:

$$\tilde{I}_2(\vec{x} + \delta\vec{x}) = \tilde{I}_1(\vec{x}). \tag{1}$$

A linear approximation of this equation, using Taylor series at first order on the left hand side, gives:

$$\begin{aligned}\xi(\vec{x}, \delta\vec{x}) &= \tilde{I}_2(\vec{x} + \delta\vec{x}) - \tilde{I}_1(\vec{x}) \\ &= \tilde{I}_2(\vec{x}) + \nabla\tilde{I}_2 \cdot \delta\vec{x} - \tilde{I}_1(\vec{x}),\end{aligned}$$

which leads to a formula similar to (24):

$$\nabla\tilde{I}_2 \cdot \delta\vec{x} + \tilde{I}_2(\vec{x}) - \tilde{I}_1(\vec{x}) = \xi(\vec{x}, \delta\vec{x}). \tag{2}$$

This formulation is used by Lucas & Kanade (1981), where the time variable does not appear explicitely. The motion vector is then defined as $\vec{v} = \delta\vec{x}/\delta t$, where δt is the time distance between two images $\tilde{I}_1$ and $\tilde{I}_2$. This approach leads to the same equation as the PDE formulation (see Sect. A), so that in practice they are equivalent.

2.2.2 Optical Flow Computation

In the original Lucas & Kanade (1981) optical flow estimation, in order to solve the aperture problem, an assumption of uniformity is made on the velocity vector: $\vec{v}$ has to be uniform over a local neighborhood (see Fig. 2). The set of OFCE equations over this neighborhood Ω yields to a linear system, where the unknowns are the two parameters of the deformation (the motion vector). The linear system can be solved using a weighted linear least-squares method (Press et al., 1992).

The local uniformity assumption (LUA) The local uniformity assumption proposed by Lucas & Kanade (1981) states that Eqs. (2) or (24) should be true locally around the location estimation, that is over a finite domain or neighborhood $\Omega(\vec{x}, s)$ centered on $\vec{x}$ and of size (or scale) ω. If $\Omega(\vec{x})$ contains $N > 2$ pixels, this assumption provides more equations of type (2) than unknowns δx_i so that the system can be solved.
The LK optical flow is the least-square (LS) minimizer of ξ in (2) on Ω.

$$\delta\vec{x}_{LS}(\vec{x}) = \arg\min_{\delta x} \|\xi(\delta\vec{x})\|^2_{\Omega(\vec{x})}, \tag{3}$$

where $\|\xi(\delta\vec{x})\|^2_{\Omega(\vec{x})} = \sum_{i=1}^{N} \xi(\vec{x}_i, \delta\vec{x})^2 = \xi^T\xi$ is the l^2 vector norm of $\mathbb{R}^N$ corresponding to the finite neighborhood $\Omega(\vec{x})$. This solution is the maximum likelihood estimator when the residual term ξ is a random variable following a gaussian distribution $N(0, \sigma^2_\xi)$. In practice, we assign coefficients to each pixel, or equivalently to each optical flow equation in the neighborhood $\Omega(\vec{x})$, so that the pixel at the center has a greater statistical weight than at the boundaries of $\Omega(\vec{x})$. For that we use the Mahalanobis distance

$$\|\xi\|^2 = \xi^{\mathrm{T}} V_\xi^{-1} \xi,$$

which allows to assign weights to each pixels $\vec{x}_i$. It is equivalent to minimizing $\|w \star \xi\|^2$ where $\star$ represents the $2D$ convolution operator and w is the weighting function. In our application w is an isotropic gaussian function normalized so that $\|w\|^2 = 1$.

LK solution to optical flow We introduce the notation $f_x = \partial f/\partial x$. Solving Eq. (3) is equivalent to finding the solution of the linear system

$$A\delta\vec{x} = b, \tag{4}$$

where:

$$A = \begin{bmatrix} \tilde{I}_{2x}(\vec{x}_1) & \tilde{I}_{2y}(\vec{x}_1) \\ \vdots & \vdots \\ \tilde{I}_{2x}(\vec{x}_N) & \tilde{I}_{2y}(\vec{x}_N) \end{bmatrix},$$

$$b = \begin{bmatrix} -(\tilde{I}_2 - \tilde{I}_1)(\vec{x}_1) \\ \vdots \\ -(\tilde{I}_2 - \tilde{I}_1)(\vec{x}_N) \end{bmatrix}.$$

The LS solution is:

$$\delta\vec{x}_{LS} = (A^{\mathrm{T}} V_\xi^{-1} A)^{-1} A^{\mathrm{T}} V_\xi^{-1} b, \tag{5}$$

where $V_\xi = E[\xi^{\mathrm{T}}\xi]$, is the covariance matrix of the residual error. The covariance matrix of $\delta\vec{x}_{LS}$ is given by:

$$V_{\delta\vec{x}} = (A^{\mathrm{T}} V_\xi^{-1} A)^{-1}. \tag{6}$$

In the rest of this report, we will note this covariance matrix as $V_{\hat{\delta\vec{x}}}$ and we will use it to define our criterion for the quality of the estimation. Indeed the diagonal elements of $V_{\hat{\delta\vec{x}}}$ are the variance of the estimation parameters. The LS estimator converges to the correct solution if the following conditions are satisfied: $E[\xi] = 0$ and $V_\xi = \sigma_\xi^2 I$, plus an additional constraint on the matrix A: $\det A^{\mathrm{T}} A \neq 0$.

Blank Wall and Aperture The *blank wall* effect occurs in $1D$ when all the $\partial I/\partial x$ term vanishes, *i.e.* when the signal gradient is null over the neighborhood. Then it is not possible to estimate a motion vector, even if the object is moving. In $2D$, the matrix singularity $\det A^{\mathrm{T}} A = 0$ means either that the image has a uniformly vanishing $2D$ gradient, which is the $2D$ *blank wall*, or that the image has a unidirectional anisotropic structure. For that reason, the matrix $A^{\mathrm{T}} A$ characterizes the *gradient texture* of the image within a given neighborhood Ω. Furthermore one equation is not enough anyway to derive the two variables of the motion vector $\delta\vec{x}$. This is the *aperture* problem. We need at least one extra constraint to carry out locally the estimation, namely in our case, the local uniformity assumption.

2.2.3 Symmetric Optical Flow Analysis (SOFA)

We opt for a symmetric formulation of the optical flow that can involve a prior information, or constraint, on the flow $\delta\vec{x}$. To impose symmetry in the

optical flow estimation, we combine the two reciprocal equations:

$$\begin{aligned}\tilde{I}_2(\vec{x}+(\delta\vec{x}-\delta\vec{x}_{th})) &= \tilde{I}_1(\vec{x}),\\ \tilde{I}_1(\vec{x}-(\delta\vec{x}-\delta\vec{x}_{th})) &= \tilde{I}_2(\vec{x}).\end{aligned}$$

We linearize both equations assuming that $\delta\vec{x}_{th}=\vec{0}$. It is possible to impose a predetermined $\delta\vec{x}_{th}$, for instance the theoretical differential rotation. We get:

$$\nabla\tilde{I}_2\cdot\delta\vec{x}+\tilde{I}_2(\vec{x})-\tilde{I}_1(\vec{x}) = \vec{\xi}_1, \quad (7)$$

$$\nabla\tilde{I}_1\cdot\delta\vec{x}+\tilde{I}_2(\vec{x})-\tilde{I}_1(\vec{x}) = \vec{\xi}_2. \quad (8)$$

We note:

$$\tilde{I}_M=\frac{\tilde{I}_1+\tilde{I}_2}{2} \quad \text{(average)},$$

$$\tilde{I}_D=\tilde{I}_2-\tilde{I}_1 \quad \text{(difference)}.$$

Adding and substracting (7) and (8)), we obtain:

$$2\times\left(\nabla\tilde{I}_M\cdot\delta\vec{x}+\tilde{I}_D(\vec{x})\right) = \vec{\xi}_1+\vec{\xi}_2, \quad (9)$$

$$\nabla\tilde{I}_D\cdot\delta\vec{x} = \vec{\xi}_1-\vec{\xi}_2. \quad (10)$$

The goal of the algorithm is to minimize a cost function $\|\xi\|^2$ now redefined, using the parallelogram identity, as:

$$\|\xi\|^2=\frac{1}{2}(\|\xi_1\|^2+\|\xi_2\|^2)=\|\frac{\xi_1+\xi_2}{2}\|^2+\|\frac{\xi_1-\xi_2}{2}\|^2. \quad (11)$$

We note $\hat{\delta\vec{x}}=\delta\vec{x}_{LS,sym}$ the vector that minimizes the quantity $\arg\min_{\delta\vec{x}}\|\xi(\delta\vec{x})\|^2_\Omega$. We can interpret this new minimization either as a generalized Tikhonov regularization or in the Bayesian framework. The advantage of this method is that the constraint (seen as a regularization constraint or a prior distribution) is derived from the data (the matrix M) and does not require any extra arbitrary parameter. Furthermore the estimation is symmetric: the parameters that minimize $\|\xi\|^2$ do not depend on the ordering between I_1 and I_2. We note:

$$A = \begin{bmatrix} \tilde{I}_{M,\vec{x}}(\vec{x}_1) & \tilde{I}_{M,y}(\vec{x}_1) \\ \vdots & \vdots \\ \tilde{I}_{M,\vec{x}}(\vec{x}_N) & \tilde{I}_{M,y}(\vec{x}_N) \end{bmatrix},$$

$$b = \begin{bmatrix} -\tilde{I}_D(\vec{x}_1) \\ \vdots \\ -\tilde{I}_D(\vec{x}_N) \end{bmatrix},$$

$$M = \frac{1}{2}\begin{bmatrix} \tilde{I}_{D,\vec{x}}(\vec{x}_1) & \tilde{I}_{D,y}(\vec{x}_1) \\ \vdots & \vdots \\ \tilde{I}_{D,\vec{x}}(\vec{x}_N) & \tilde{I}_{D,y}(\vec{x}_N) \end{bmatrix}.$$

where I_x means $\partial I/\partial x$.
The cost function $\|\vec{\xi}\|^2$ can be written as:

$$\|\vec{\xi}\|^2 = \frac{1}{2}\left(\|A\delta\vec{x} - b\|^2 + \|M\delta\vec{x}\|^2\right) = \frac{1}{2}\left(\|A\delta\vec{x} - b\|^2 + \|\delta\vec{x}\|^2_{M^{\mathrm{T}}M}\right). \quad (12)$$

In the Bayesian framework, it appears that imposing the symmetry is equivalent to adding a prior constraint to the vector $\delta\vec{x}$. Using the Bayes' theorem, we interpret Eq. (11) as the following conditional probability:

$$\Pr(\delta\vec{x}|I_D) = \frac{\Pr(I_D|\delta\vec{x}) \times \Pr(\delta\vec{x})}{\Pr(I_D)}, \quad (13)$$

where

$$\Pr(I_D|\delta\vec{x}) \propto \exp\left(-\frac{1}{2}(A\delta\vec{x} - b)^{\mathrm{T}}V_\xi^{-1}(A\delta\vec{x} - b)\right), \quad (14)$$

$$\Pr(\delta\vec{x}) \propto \exp\left(-\frac{1}{2}\delta\vec{x}^{\mathrm{T}}(M^{\mathrm{T}}V_\xi^{-1}M)\delta\vec{x}\right). \quad (15)$$

Indeed Eq. (10) can be used to define a prior distribution on $\delta\vec{x}$. This prior distribution plays a role when the gradient texture is deformed, and the two diagonal elements $M^{\mathrm{T}}M$ then represent the deformation rates along the x and y axes. When the gradient texture is deformed between I_1 and I_2, because of occlusion or strong deformation (due for instance to heatings), then estimation is forced to tend to the displacement vector used in the linearization (here $\vec{x}_{th}$ is the $\vec{0}$ vector). Basically, it stabilizes the estimation towards the reference value (null displacement but could be the differential rotation for instance) when the gradient texture is modified between I_1 and I_2. Finally, we get the solution:

$$\hat{\delta\vec{x}} = (A^{\mathrm{T}}V_\xi^{-1}A + M^{\mathrm{T}}V_\xi^{-1}M)^{-1}A^{\mathrm{T}}V_\xi^{-1}b. \quad (16)$$

The covariance matrix of $\delta\vec{x}$ is now:

$$V_{\delta\vec{x},\mathrm{sym}} = (A^{\mathrm{T}}V_\xi^{-1}A + M^{\mathrm{T}}V_\xi^{-1}M)^{-1}. \quad (17)$$

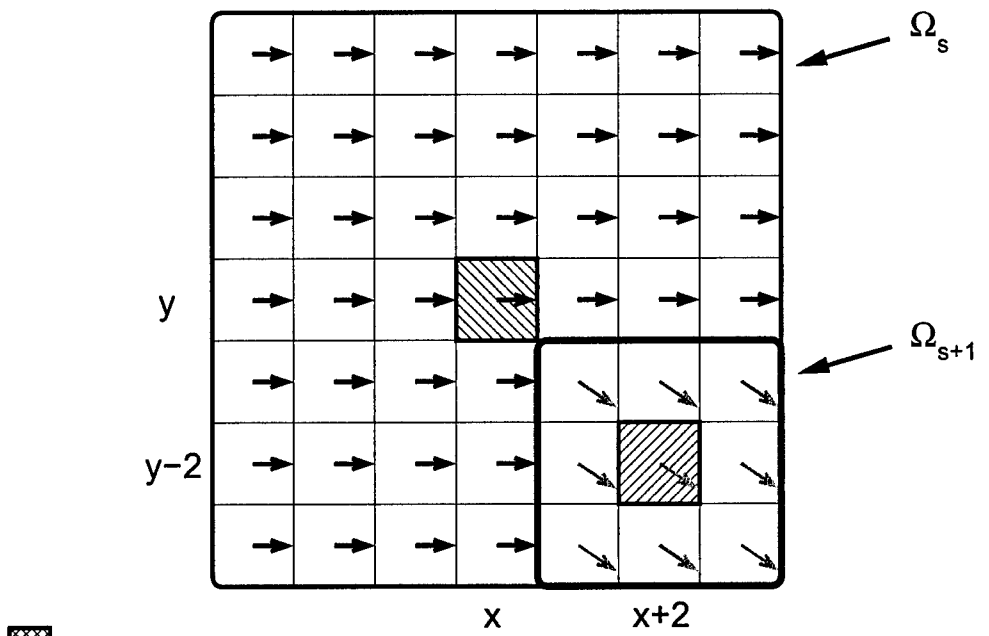

Figure 2: The local uniformity assumption in the multiscale estimation process with an update between scale $s+1$ and scale s. At the lower left corner, the estimation at location $(x+2, y-2)$ is updated because the quality Q has been improved (see Sect. 2.3.1).

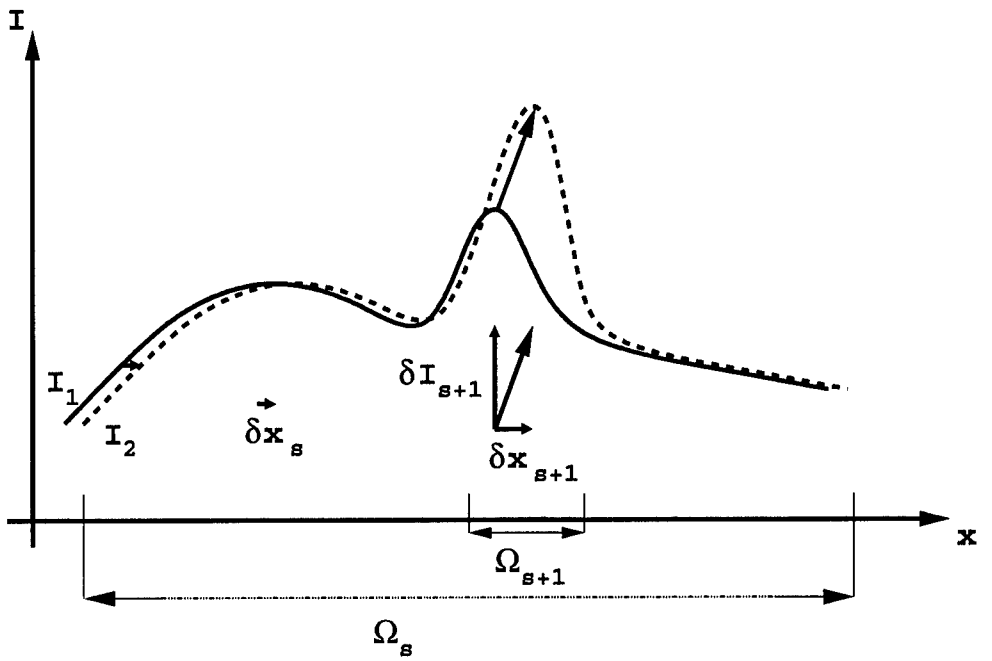

Figure 3: 1D example of an updating step in the multiscale MoVaTrac algorithm. At scale $s+1$, the estimation is updated from $(\delta x_s, \delta I_s)$ to $(\delta x_{s+1}, \delta I_{s+1})$.

2.2.4 Brightness Variation Estimation

We extend the OFCE with δI, that estimates the brightness variation between the two images, relaxing the BCA assumption. This approach has been suggested by Lucas & Kanade (1981) and has been recently used by several authors (e.g. Odobez & Bouthemy, 1995; Periaswamy & Farid, 2003). An example of a one dimensional signal undergoing a translation plus a brightness variation is shown in Fig. 3. The BV map can be interpreted as the variation of LOS emission parameters (temperature and density).

The symmetric optical flow equation (9) becomes (without the residual term ξ):

$$\nabla \tilde{I}_M \cdot \delta\vec{x} + \tilde{I}_D + \delta I = 0, \tag{18}$$

where $\delta I = \alpha \times c_I$. The quantity α is a parameter measuring the amount of variation ΔI of intensity as a function of the pixel unit Δx. It affects the estimation covariance matric but not the estimation itself. It modifies the dynamics of the estimated parameter c_I. From now on, we will note $\theta = (\delta x, \delta y, c_I)^{\mathrm{T}}$ the vector of parameters that we want to estimate.

2.3 The multiscale SOFA computation

In order to make the maps $(\delta x, \delta y)$, which corresponds to the velocity vector map, and δI (bv) as local as possible, we compute the optical flow in a multiscale framework (see Fig. 4). The scale is defined by the scale parameter s of the function w (see Sect. 2.2.2). The first computation is carried out at a predefined large scale s_0. At this scale, a large number of pixels are used in the estimation. This estimation may nevertheless be strongly biased. Furthermore, within a large neighborhood (*i.e.* at large scale), the hypothesis made on the optical flow (extended BCA and LUA) are no longer valid. To compensate for this effect, we add a multiscale updating step. It consists in an update of the parameter estimation, from the upper scale s_0 to a lower scale, if the quality index Q of the estimation has increased. In other terms, there is an update when the quality at the smaller scale $s+1$ is higher than the current larger scale s. From our definition of the quality index Q (see Sect. 2.3.1 for details), we know that if the texture and the similarity have been improved from s to $s+1$, then there is an update. We also leave as an option in our implementation the propagation of the large scale velocity to the lower scale, inducing some stiffness between features across scales, *i.e.* when finer scales undergo the motions of large scales. Combined with an multiresolution pyramid approach, it gives the possiblity to handle larger motions (more than $\sim$ 1.5 pixels).

2.3.1 Quality index

Contrary to global methods such as Horn & Schunck (1981), our optical flow approach gives the possibility to carry out the registration depending on the neighborhood content. For that reason, we define an index Q (for "quality"). We will use this index for:

- interscale comparison in order to find the best scale of estimation in the multiscale implementation by comparing Q between successive scales,
- interpixel comparison the pixels that have the best estimation by ordering the pixels according to the Q-criterion.

In order to illustrate the meaning of Q, we can use the space of parameter θ. If we assume $V_\xi = \sigma_\xi^2 I$ and since $A^{\mathrm{T}}A$ is symmetric, we can write $A^{\mathrm{T}}A = PDP^{\mathrm{T}}$ with $P^{\mathrm{T}} = P^{-1}$, which gives:

$$V_{\delta\vec{x}}^{-1} = \frac{1}{\sigma_\xi^2} PDP^{\mathrm{T}}$$

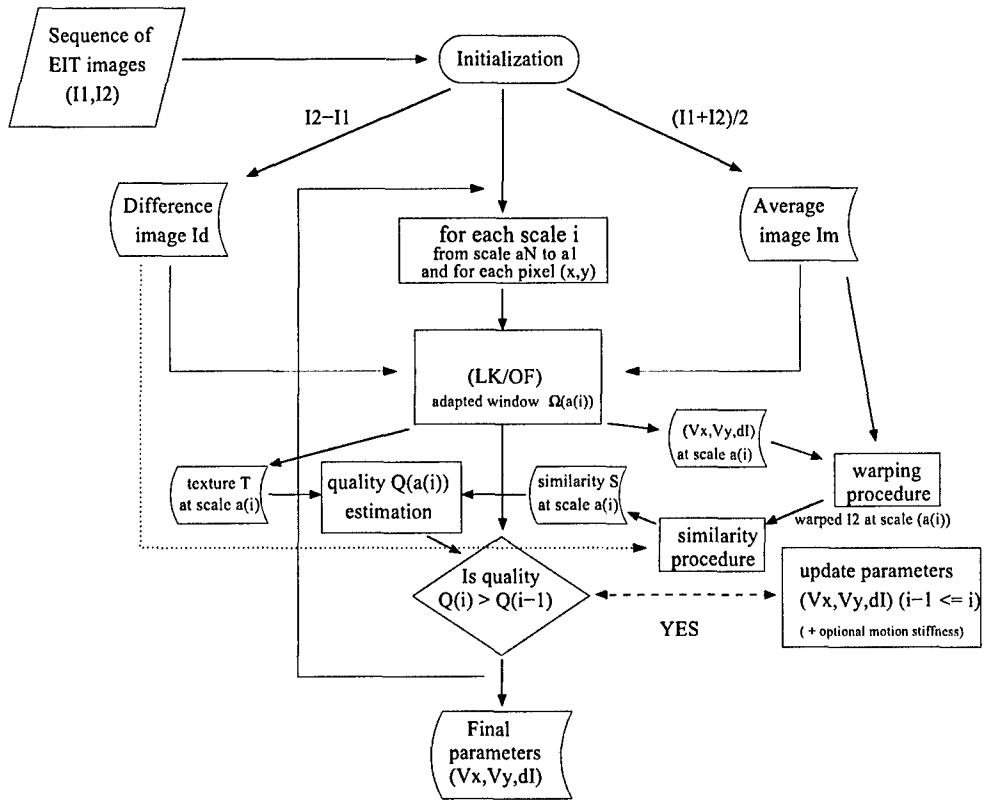

Figure 4: Description of the MoVaTrac algorithm.

$$D = \begin{bmatrix} \lambda_1 & & \\ & \lambda_2 & \\ & & \lambda_3 \end{bmatrix}.$$

We then define our quality index as:

$$\begin{aligned} Q &= \min \text{eigenvalue} \left(V_{\delta\vec{x}}^{-1} \right), \\ &= \frac{1}{\sigma_\xi^2} \times \min(\lambda_1, \lambda_2, \lambda_3). \end{aligned}$$

If we note $S = \frac{1}{\sigma_\xi^2}$ and $T = \min(\lambda_1, \lambda_2, \lambda_3)$, we finally obtain:

$$Q = S \times T. \tag{19}$$

where S can be seen as the similarity between both images after deformation, while T quantifies the amount of texture in the observation window. Indeed, we have :

$$S = \frac{1}{\sigma_\xi^2}, \tag{20}$$

where

$$\sigma_\xi^2 = \sum_{x_i \in \Omega} w_i^2((I_2 + \alpha\delta I)(x_i + \delta x) - I_1(x_i))^2. \tag{21}$$

S^{-1} is an estimation of the quantity σ_ξ^2. As the noise on images I_1 and I_2 is supposed to be gaussian white noise $N(0, \sigma_I^2)$, σ_ξ^2 can be interpreted as an estimation of $2\sigma_I^2$. This estimator has well-known statistical properties that can be used for statistical tests. It is also bounded by the dynamics of the signal. To check the numerical stability of the matrix $A^T A$, we compute its eigenvalues λ and look at the minimum eigenvalue λ_{min}. In fact, this quantity corresponds to a " texture " criterion. It is homogeneous with $\sum I_x^2$, which indicates that it is high when the texture is well suited to the motion analysis. It is low when there is a blank wall effect or a strong aperture. For this reason we define a "texture" index T equal to $\lambda_{min} = \min(\lambda_1, \lambda_2, \lambda_3)$.

2.3.2 Updating through scales

The variance σ_ξ^2 of the residual is estimated by the dissimilarity quantity σ_ξ^2 and the similarity is equal to the inverse of S. Two conditions have to be respected for a reliable matching (Shi & Tomasi, 1994): first the signal "texture"' (T) must be sufficient (no aperture, that is enough "texture"), and second the matching measured by similarity S must be acceptable after the

estimated deformation. Both conditions are satisfied when the quality index Q is high, where the term "high" will be quantified in the calibration phase. When T is low (unadapted texture, blank wall), then S can still be high and meaningless. If S is low, and T is high, the quality is low but the estimation is then indeed incorrect.
$T = \lambda_{min}$ is the texture parameter, and S is a measure of similarity between the first image and the second image after warping. If T is large, then the quality is high because the texture of the signal enables motion analysis (no aperture problem). If the similarity is low, then the quality is penalized because the registration (comparison of deformed image I_2, warped into reference frame of image I_1), and image I_1 is bad (high dissimilarity σ_ξ^2).

Our quality criterion Q is related to the theoretical standard deviations of the parameters given by a linear least-squares fit.

The updating stape corrects locally the error on velocity estimation but increases the variance of the estimation because there are less pixels contributing to the estimation. The updating phase enables a tradeoff between large scales, where the bias is due to the non uniformity of the deformation, and small-scales, where the variance of estimation is due to the low number of pixels (low N). In our computations, the set of scales is a sampling of four scales. A higher number of scales only improves the estimation and removes the threshold effect due to the updating step. For a large number of scales, the parameter maps (velocity, brightness variations and quality index) are smooth. The flowchart of the algorithm is shown in Fig. 4.

2.3.3 Error Analysis

Our residual term may not be gaussian for the following reasons:

- non-gaussian noise implying a non gaussian residual distribution (statistical error): e.g. poisson noise, spatial noise : intrapixel activity caused by sub-pixel motions, can be due to transparency effect can cancel the advection effect at small scales. For instance there could be subpixel opposite motion of two structures, which mixture will yield to outlying pixels,

- modelling error (non-zero second or higher order terms): motions more complex than translation, non uniform intensity variations, presence of non negligible higher order terms in Eq. (2) (systematic error),

- noise in the matrix A due to noisy spatial gradient estimations.

2.4 Postprocessing: coordinate transform rotation velocity and meridional motions

After estimating the velocity parameters $v_x = \delta x/\delta t$ and $v_y = \delta y/\delta t$, we project them on heliospheric coordinates, to get the rotation velocity and the meridional velocity. In this report, we only use the synodic observation. The observed synodic rotation velocity (observed from SoHO or from the Earth) is corrected to get the sidereal velocity, for a comparison of the rotation velocities that we find. We first transform the spatial coordinates into heliospheric coordinates.

3 Calibration

3.1 Synthetic images

We test the efficiency of our algorithm on a couple of images. The first image is shown in Fig. 5.

$$G(\vec{x}, \vec{\mu}_i, \sigma_i, A_i) = A_i \exp(-\frac{|\vec{x} - \vec{\mu}_i|^2}{2\sigma_i^2}) \ , \ i = 0, 7$$

The parameters $\vec{\mu}_i$,σ_i,A_i have been generated randomly in order to produce an image that is similar to an EIT image.

In Fig. 6 we see that above a predefined threshold q, the objects are well located and the estimated motion parameters are correctly estimated (same for bv, not show here).

3.2 Semi-artificial EIT sequences

We calibrate our method on semi-artificial solar sequences. We apply a displacement field to an EIT image I_1 and we obtain a second image $I_{1,dr}$ using a parametric model of differential rotation estimated by Vršnak et al. (2003). The interpolation procedure is based on the IDL function of cubic interpolation (Park & Schowengerdt, 1983). This method uses cubic polynomials to approximate the optimal sinc interpolation function. Due to spatial aliasing, this method gives bad results when there are high spatial frequencies since it assumes that the signal is band-limited (DeForest, 2004). This effect lowers the similarity term S, since the image pattern is not correctly deformed and the simple model of deformation (local translation and constant bv) is no longer valuable. The measurements are then projected back into rotational motions and meridional motions. In Fig. 7 we compare the extracted rotation velocity with the curve of the theoretical rotation. Each bin is 0.5

degree per day wide and 1 degree in latitude high. The relative dispersion around the theoretical rotation is approximatively $\pm$ 5 %. This value will to be compared with the discrepancy that we find on the real sequences (Sec. 4).

4 EIT Sequence Analysis

Three successive images are observed on the 1998-05-03, repectively at times 21:00:21 (I_1), 21:12:09 (I_2) and 21:25:35 (I_3) in the CME Watch mode, at the wavelength 19.5 nm (see Fig. 1). A second sequence of two images (J_1, J_2) observed on the 1999-04-17, repectively at times 00:12:10 (J_1) and 00:24:42 (J_2). We run the algorithm on rebinned images with resolution 512 $\times$ 512 pixels to reduce the computation time. We choose 5 quality bins that segment the solar disk into 5 sets of equal number of pixels.

4.1 Differential Rotation Analysis

We analyse the sequence (J_1, J_2) in the same conditions of section 3. Figure 8 shows the density of pixels that have the highest estimation quality (levels 4 and 5), according to their latitude and their velocity rotation. We also plot the theoretical rotation (plain line). The estimated velocities are variable (up to $\pm$ 2 degrees per day).

We note that for the quality level 4, the rotation velocities of the two couples are $\sim$ 10 % lower than the expected curve.

Figure 9 (left), the subsampled velocity is displayed. After examining the histograms (Fig. 8), we retrieve the cluster of pixels that have a fast rotation velocity (latitude range : 30 to 40 degrees). A zoom on a particular region belonging to this cluster, with high quality estimation (level 5) and high rotation velocity (above 15 degrees per day) is displayed on the right, and for which we choose to overplot a greater density of arrows.

4.2 Brightness Variation Maps

Figure 10 shows the BV maps of the two successive couples of images (I_1, I_2) and (I_2, I_3), limited to the ondisc pixels. In the latter, an obvious change in brightness is observed. In this example, the thresholds are obvious to choose in order to detect brightenings from the histogram (Fig. 11). The same for dimmings or negative brightness variations. This will be made using a set of selected sequences containing typical eruptive events. In the sequence

(images I_1, I_2), we have some precursors in the BV maps have been identified in the active regions.

Figure 11 (left), the plain line shows peaks (intensity greater than 1) of outstanding brightness variations. These peaks are hardly visible in the difference image, because of the motion effect, which motivated the use of this technique to process long sequence of EIT images (typically one day of observations) and extract the interesting but faint brightness variation areas from the bv histogram. In the right figure, the extracted region is outlined over the difference image.

5 Conclusion

Real and semi-artificial EIT sequences have been analysed in terms of motions and brightness variation over the full solar disc. This estimation is dense (one estimation for each pixel), but a quality level is assigned to each pixel. When this index is high, the estimation is reliable. A multiscale implementation refines the estimation from coarse scale to fine scales. For each pixel, when the quality estimated at one scale increases at the finer scale, then the estimation is updated. Thus the algorithm has a preference for coarse scale estimations, that are kept through the multiscale refinement unless the quality of the estimation is locally improved. At coarse scales, the number of pixels used in the estimation is higher than at finer scales: the estimation is more robust. In the velocity maps, and for high quality levels (4 and 5), we observe accumulations of pixels into clusters that have a common rotation velocity. Using the histogram (Fig. 8), we have identified pixels from an active region (figure 9). We now want to know how variable is the rotation velocity of the active region over half a rotation. This will be possible after the processing of longer sequences (several days). The variations around the rotation velocity could be interpreted as oscillations around the theoretical and global differential rotation. The systematic analysis the EIT archive will help us confirm this result. Furthermore a full disc analysis of our algorithm enables an operational detection of events in sequences of two coronal EUV images, using the BV maps. In the sequence of 1998-05-03, a strong brightening covering a large area has been undoubtedly singled out from the regular solar activity. On the other hand, this event is classified as an EIT wave. The analysis of the histogram of the BV map shows peaks deviating from regular BV histograms. We will use this criterion to extract outstanding intensity variations in long sequence of EIT images. A future objective of this is to associate motions and brightness variations with coronal events defined by observers. We will also investigate the correlations in

time between the outstanding estimations (fast motions, strong brightness variations), and their localizations, and the in-situ measurements (LASCO CMEs and in-situ ACE data) and other space weather observations relevant to event prediction. This work leads to solar physics research as well as real time space weather services.

A PDE formulation of the optical flow

The PDE approach considers the image intensity $I(\vec{x}(t), t)$ as a physical quantity that is conserved over time, where $\vec{x} = (x, y)^{\mathrm{T}}$ is the spatial position in the image plane. The PDE form of the BCA is:

$$\frac{dI}{dt} = 0. \tag{22}$$

The differentiation of $I(\vec{x}(t), t)$ in Eq. (22) gives the OFCE:

$$\nabla I \cdot \vec{v} + \frac{\partial I}{\partial t} = 0, \tag{23}$$

where $\vec{v} = (dx/dt, dy/dt)^{\mathrm{T}}$ is the velocity vector of the apparent motion.

As the real signals are discretized, the temporal and spatial derivatives must be approximated. We use hereafter the finite difference scheme to compute the *temporal* derivative $\partial I/\partial t$ using the difference image $\delta I = I_2 - I_1$ and the time distance δt between I_1 and I_2:

$$\frac{\partial I}{\partial t} = \lim_{\Delta t \to 0} \frac{I(\vec{x}, t + \Delta t) - I(\vec{x}, t)}{\Delta t} \simeq \frac{\delta I}{\delta t} + o(\delta t \frac{\partial^2 I}{\partial t^2}).$$

The discretized OFCE is:

$$\nabla \tilde{I} \cdot \vec{v} + \frac{\delta \tilde{I}}{\delta t} = \xi(\vec{x}, \delta t), \tag{24}$$

where $\delta \tilde{I} = \tilde{I}_2(\vec{x}) - \tilde{I}_1(\vec{x}) = g_a \star \delta I$. The order of the discretization error (different from the model error) is (see Press et al., 1992):

$$\xi(\vec{x}, \delta t) \sim \delta t \frac{\partial^2 \tilde{I}}{\partial t^2}.$$

In this first approach, the spatial derivatives can be computed from either image I_1 and/or I_2. In the case of image registration, the order of error due to the truncation of higher order terms is:

$$\xi(\vec{x}, \delta \vec{x}) \sim \delta \vec{x}^{\mathrm{T}} H_{\tilde{I}} \, \delta \vec{x},$$

where $H_{\tilde{I}}$ is the Hessian matrix of $\tilde{I}$.

References

Barron, J., Fleet, D., Beauchemin, S., & Burkitt, T. 1992, CVPR, 92, 236

Black, M. & Anandan, P. 1993, in ICCV93, 231–236

Brajša, R., Wöhl, H., Vršnak, B., et al. 2001, A & A, 374, 309

De Groof, A., Berghmans, D., van Driel-Gesztelyi, L., & Poedts, S. 2004, A & A, 415, 1141

DeForest, C. E. 2004, Solar Physics, 219, 3

Deforest, C. E. & Gurman, J. B. 1998, ApJ, 501, L217+

Delaboudiniere, J.-P., Artzner, G. E., Brunaud, J., et al. 1995, Solar Physics, 162, 291

Gissot, S. F., Hochedez, J.-F., Dibos, F., et al. 2003, in ESA SP-535: Solar Variability as an Input to the Earth's Environment, 853–856

Handy, B. N., Acton, L. W., Kankelborg, C. C., et al. 1999, Solar Physics, 187, 229

Hochedez, J. F., Zhukov, A., Robbrecht, E., et al. 2005, Annales Geophysicae, 23, 3149

Horn, B. & Schunck, G. 1981, Artificial Intelligence, 17, 185

Hudson, H. S. & Cliver, E. W. 2001, J. Geophys. Res., 25199

Klimchuk, J. A., Tanner, S. E. M., & De Moortel, I. 2004, ApJ, 616, 1232

Krijger, J. M. & Roudier, T. 2003, A & A, 403, 715

Krijger, J. M., Roudier, T., & Rieutord, M. 2002, A & A, 387, 672

Kucera, T. A., Tovar, M., & De Pontieu, B. 2003, Solar Physics, 212, 81

Longcope, D. W. 2004, ApJ, 612, 1181

Lucas, B. & Kanade, T. 1981, in IJCAI81, 674–679

Moses, D., Clette, F., Delaboudiniere, J.-P., et al. 1997, Solar Physics, 175, 571

Noglik, J. B., Walsh, R. W., & Ireland, J. 2005, A & A, 441, 353

November, L. J. & Simon, G. W. 1988, Astrophysical Journal, 333, 427

Odobez, J.-M. & Bouthemy, P. 1995, Journal of Visual Communication and Image Representation, 6, 348

Oraevsky, V. N. & Sobelman, I. I. 2002, Astronomy Letters, 28, 401

Park, S. & Schowengerdt, R. 1983

Periaswamy, S. & Farid, H. 2003, IEEE Transactions on Medical Imaging, 22, 865

Press, W. H., Teukolsky, S. A., Vetterling, W. T., & Flannery, B. P. 1992, Cambridge: University Press

Rosner, R., Tucker, W. H., & Vaiana, G. S. 1978, ApJ, 220, 643

Roudier, T., Rieutord, M., Malherbe, J. M., & Vigneau, J. 1999, A & A, 349, 301

Schrijver, C. J., Title, A. M., Berger, T. E., et al. 1999, Solar Physics, 187, 261

Shi, J. & Tomasi, C. 1994, in IEEE Conference on Computer Vision and Pattern Recognition (CVPR'94), Seattle

Simoncelli, E. P. 1999, in Handbook of Computer Vision and Applications, ed. B. Jähne, H. Haussecker, & P. Geissler, Vol. 2 (San Diego: Academic Press), 397–422

Simoncelli, E. P., Adelson, E. H., & Heeger, D. J. 1991, in Proc Conf on Computer Vision and Pattern Recognition (Mauii, Hawaii: IEEE Computer Society), 310–315

Vršnak, B., Brajša, R., Wöhl, H., et al. 2003, A & A, 404, 1117

Welsch, B. T., Fisher, G. H., Abbett, W. P., & Regnier, S. 2004, ApJ, 610, 1148

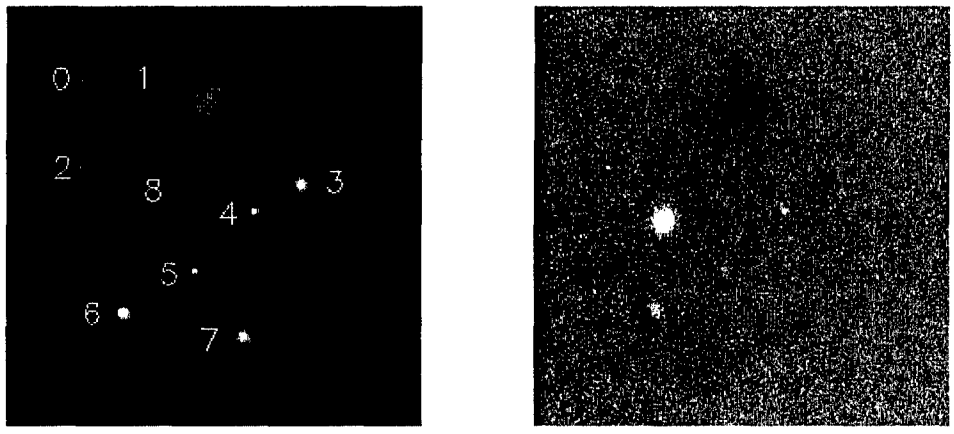

a. The gaussian objects numbered from 0 to 7. b. Diffference Image.

Figure 5: Left: image showing the 8 gaussian objects G_i with the additive white noise. Right: the difference image.

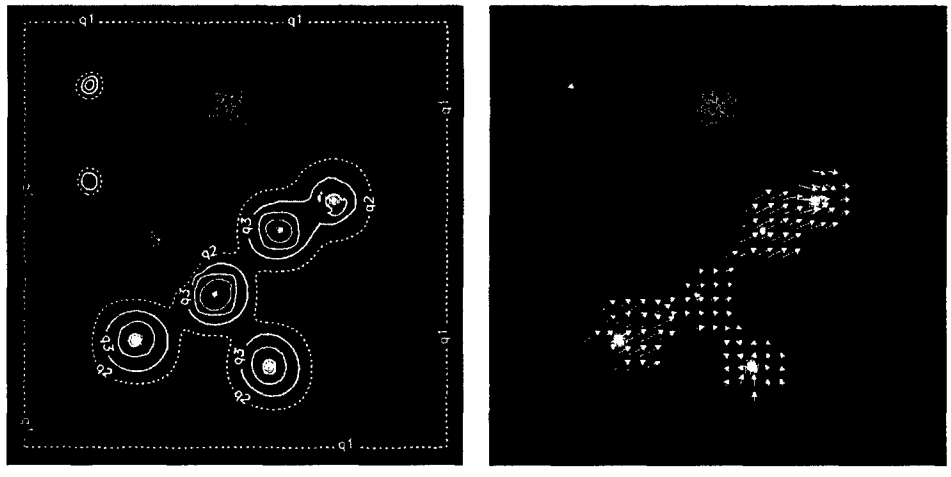

Figure 6: Left: Quality level lines. The letter q_i represents the i -level line of quality. At q1 (lowest level, dotted-dashed line), some noisy structures are still selected. The level q_2 is a dotted line, while the plain lines represent the superior levels q_3,q_4 and q_5. Right: Velocity estimation for a given quality threshold q.

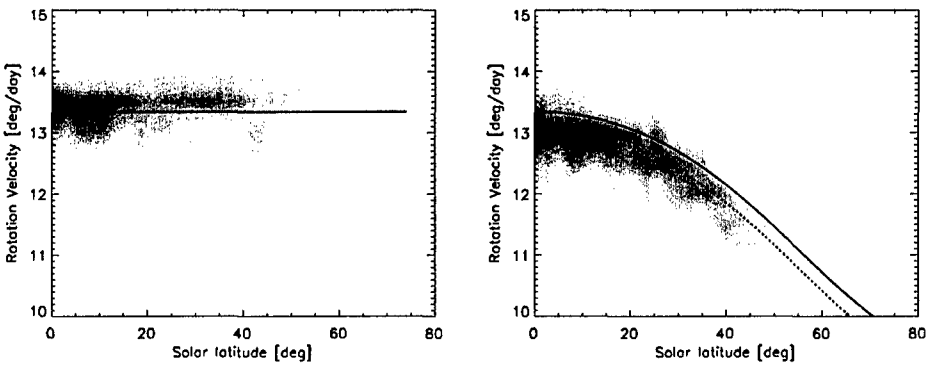

a. Rrigid rotation. b. Synthetic differential rotation.

Figure 7: Calibration procedure using semi-artificial EIT sequences on which a synthetic rotation has been applied. The grey level represents the density of solar disc pixels. Vertical axis: synodic rotation velocity (in degree per day). Horizontal axis: solar latitude (in degree).

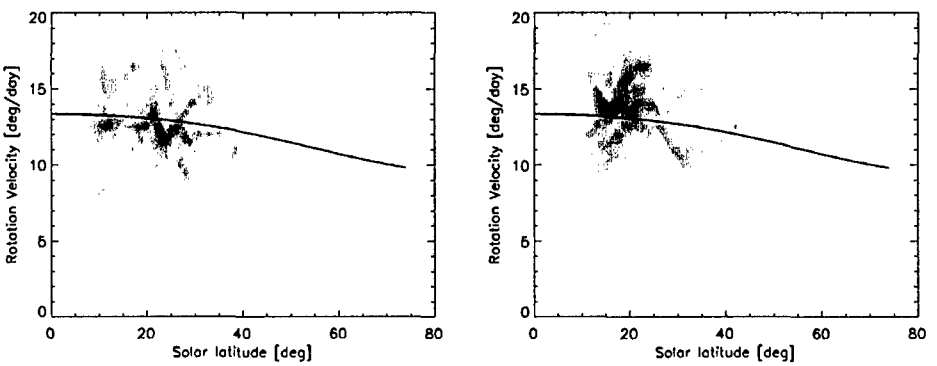

a. (J_1, J_2), q=4 b. (J_1, J_2), q=5

Figure 8: Density of solar disc pixels as a function of synodic rotation velocity (ordinate) and latitude (abciss) for quality levels 4 and 5.

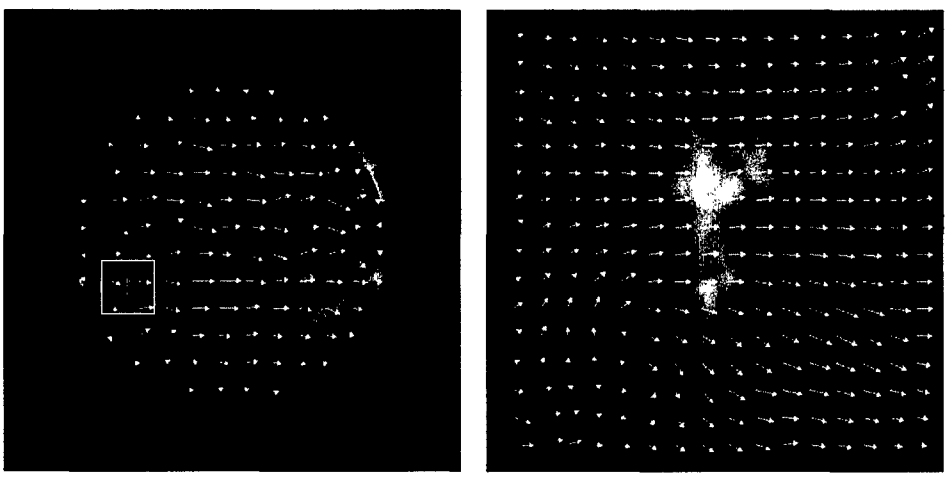

Figure 9: Left: full disc subsampled velocity field (v_x, v_y). Right: zoom on an active region with a rotation velocity greater than the expected value of the differential rotation.

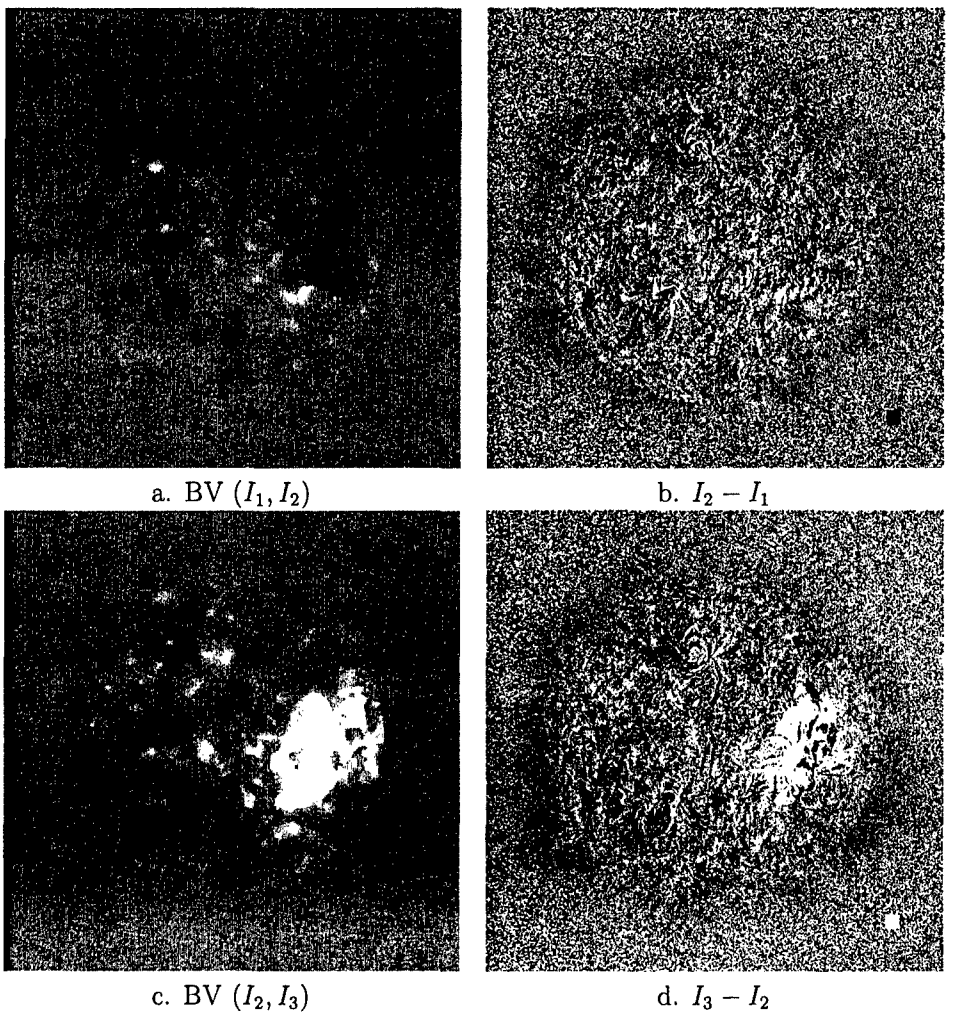

a. BV (I_1, I_2) b. $I_2 - I_1$

c. BV (I_2, I_3) d. $I_3 - I_2$

Figure 10: The two BV maps for the sequences (I_1, I_2) and (I_2, I_3) and the corresponding difference images. The grey levels have the same scale in each image.

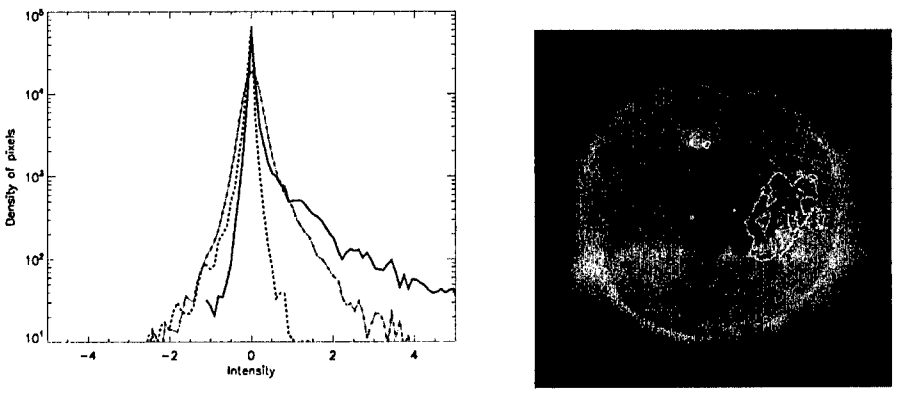

Figure 11: Left. Plain line: histogram of BV for (I_2, I_3). Dotted line: histogram of the difference image $(I_3 - I_2)$. Dashed line: histogram of BV for (I_1, I_2). Right: superimposed on I_3, the thresholded bv map of (I_2, I_3) using the threshold 1 suggested by the peaks in the BV histogram (plain line in the left figure). In this histogram, the brightness variations that are not due to the motion effect appear clearly, while they are not observed in the histogram of the difference image (dotted line).